



VERTICO and IllustrisTNG: The Spatially Resolved Effects of Environment on Galactic Gas

Adam R. H. Stevens¹, Toby Brown², Benedikt Diemer³, Annalisa Pillepich⁴, Lars Hernquist⁵, Dylan Nelson⁶, Yannick M. Bahé^{7,8}, Alessandro Boselli⁹, Timothy A. Davis¹⁰, Pascal J. Elahi¹¹, Sara L. Ellison¹², María J. Jiménez-Donaire^{3,13}, Ian D. Roberts⁸, Kristine Spekkens¹⁴, Vicente Villanueva³, Adam B. Watts¹, Christine D. Wilson¹⁵, and Nikki Zabel¹⁶

¹International Centre for Radio Astronomy Research, The University of Western Australia, Crawley, WA 6009, Australia

²Herzberg Astronomy and Astrophysics Research Centre, National Research Council of Canada, Victoria, BC, V9E 2E7, Canada; tobias.brown@nrc-cnrc.gc.ca

³Department of Astronomy, University of Maryland, College Park, MD 20742, USA

⁴Max-Planck-Institut für Astronomie, D-69117 Heidelberg, Baden-Württemberg, Germany

⁵Institute for Theory and Computation, Harvard-Smithsonian Center for Astrophysics, Cambridge, MA 02138, USA

⁶Institut für theoretische Astrophysik, Zentrum für Astronomie, Universität Heidelberg, D-69120 Heidelberg, Baden-Württemberg, Germany

⁷Institute of Physics, Laboratory of Astrophysics, Ecole Polytechnique Fédérale de Lausanne (EPFL), Observatoire de Sauverny, 1290 Versoix, Switzerland

⁸Leiden Observatory, Leiden University, P.O. Box 9513, NL-2300 RA Leiden, The Netherlands

⁹Aix-Marseille Université, CNRS, CNES, LAM, Marseille, France

¹⁰Cardiff Hub for Astrophysics Research & Technology, School of Physics & Astronomy, Cardiff University, Queens Buildings, Cardiff, CF24 3AA, UK

¹¹Pawsey Supercomputing Centre, Kensington, WA 6151, Australia

¹²Department of Physics & Astronomy, University of Victoria, Finnerty Road, Victoria, BC V8P 1A1, Canada

¹³Observatorio Astronómico Nacional (IGN), C/Alfonso XII, 3, E-28014 Madrid, Spain

¹⁴Royal Military College of Canada, P.O. Box 17000, Station Forces, Kingston, ON, K7K 7B4, Canada

¹⁵Department of Physics & Astronomy, McMaster University, 1280 Main Street W, Hamilton, ON, L8S 4M1, Canada

¹⁶Department of Astronomy, University of Cape Town, Private Bag X3, Rondebosch 7701, South Africa

Received 2023 June 30; revised 2023 September 25; accepted 2023 October 9; published 2023 November 3

Abstract

It has been shown in previous publications that the TNG100 simulation quantitatively reproduces the observed reduction in each of the total atomic and total molecular hydrogen gas for galaxies within massive halos, i.e., dense environments. In this Letter, we study how well TNG50 reproduces the *resolved* effects of a Virgo-like cluster environment on the gas surface densities of satellite galaxies with $m_* > 10^9 M_\odot$ and star formation rate $> 0.05 M_\odot \text{ yr}^{-1}$. We select galaxies in the simulation that are analogous to those in the HERACLES and VERTICO surveys and mock-observe them to the common specifications of the data. Although TNG50 does not quantitatively match the observed gas surface densities in the centers of galaxies, the simulation does qualitatively reproduce the trends of gas truncation and central density suppression seen in VERTICO in both H I and H₂. This result promises that modern cosmological hydrodynamic simulations can be used to reliably model the post-infall histories of cluster satellite galaxies.

Unified Astronomy Thesaurus concepts: [Galaxy environments \(2029\)](#); [Galaxy evolution \(594\)](#); [Interstellar atomic gas \(833\)](#); [Interstellar molecules \(849\)](#)

1. Introduction

In recent years, the realism of cosmological hydrodynamic simulations has grown to the point where the empirical effects of galaxy environment on the global gas properties of galaxies are demonstrably reproducible at low redshift (e.g., Stevens et al. 2019b; Yun et al. 2019; Stevens et al. 2021). Indeed, this is also true for some semi-analytic models of galaxy formation (e.g., Stevens & Brown 2017; Xie et al. 2020). These tests of forefront models in the literature have become possible thanks to statistically significant and representative observational surveys that have traced the emission from *both* the atomic and molecular gas in galaxies that cover the spectrum of environments from field isolation to massive galaxy clusters at low redshift (e.g., Catinella et al. 2018).

While the broad effects of environment on galaxies' gas is now reasonably well understood (see the review by Cortese et al. 2021), surveys have started directing their attention to the

gas properties on local scales inside galaxy disks. The “Virgo Environment Traced in CO” survey (VERTICO; Brown et al. 2021) has observed the molecular hydrogen gas content [H₂, traced via the CO(2–1) line] at sub-kiloparsec resolution across 51 late-type galaxies in the Virgo cluster, all of them with existing multiwavelength maps of atomic hydrogen gas (H I), stellar emission, and star formation activity. Recently, Watts et al. (2023) used this data set to show that, as galaxies are processed by the cluster, environmental mechanisms drive a continuous decrease in both H I and H₂ local surface densities ($\Sigma_{\text{H I}}$ and Σ_{H_2} , respectively) at fixed local stellar surface density (Σ_*) with respect to the field. From a theoretical perspective, it is clearly an important next step to establish if the latest simulations are capable of reproducing (i) the scaling relations of $\Sigma_{\text{H I}}$ and Σ_{H_2} values with Σ_* observed in nearby field and cluster populations and (ii) the systematic influence of environment upon those relationships.

Taking that step in this Letter, we investigate the resolved-gas scaling relations of individual galaxies from the TNG50 simulation (Nelson et al. 2019a; Pillepich et al. 2019), mock-observing them to be directly comparable to VERTICO and the

“Heterodyne Receiver Array CO Line Extragalactic Survey” (HERACLES; Leroy et al. 2009).

2. Data and Methods

2.1. Observations

The observational samples of field and cluster galaxies used in this paper are drawn from HERACLES (Leroy et al. 2009) and VERTICO (Brown et al. 2021), respectively. The analysis sample used in this paper is a superset of that used in Watts et al. (2023), and there is a detailed discussion of the observational biases present in comparing these data in that work. Briefly, the two data sets contain star-forming late-type galaxies that are well matched in global stellar mass and specific star formation rate (SFR). The H I observations for VERTICO and HERACLES galaxies are drawn from the Very Large Array Imaging of Virgo in Atomic gas survey (VIVA; Chung et al. 2009) and The H I Nearby Galaxy Survey (Walter et al. 2008), respectively. All molecular-gas information is derived from the public data cubes using the methodology described in Brown et al. (2021). Similarly, global stellar-mass and SFR estimates are drawn from the $z = 0$ Multiwavelength Galaxy Synthesis database (Leroy et al. 2019), while resolved stellar and SFR surface densities are derived from identical multiwavelength data for both surveys following the methods outlined in Villanueva et al. (2022) and Jiménez-Donaire et al. (2023), respectively. VERTICO is typically 2–3 times more sensitive than HERACLES in both H I and H₂ densities, which ensures that any observed differences with environment are not driven by sensitivity differences between the surveys.

For this work, we select we only select galaxies with stellar mass $m_* > 10^9 M_\odot$ and inclinations less than 70° , ensuring the galaxies’ surface density maps can be reliably deprojected with a simple cosine-of-inclination correction factor. These selections yield a final resolution-matched sample consisting of 10 field galaxies from HERACLES and 33 cluster galaxies from VERTICO. These galaxies all have star formation rates $\text{SFR} \gtrsim 0.05 M_\odot \text{yr}^{-1}$.

Very briefly, each galaxy has molecular gas, stellar mass, and SFR surface density maps that have been smoothed to a spatial resolution of ~ 1.2 kpc with a pixel size of ~ 650 pc to approximately Nyquist-sample the smoothing kernel [or CO(2–1) resolving beam]. This approximately matches the resolution of the H I data from VIVA (including an update where the D-configuration data were removed, leaving only the higher-resolution C-configuration data). The derived data products for VERTICO and HERACLES are produced using a near-identical procedure to that described in Brown et al. (2021) for the molecular-gas surface densities, in Jiménez-Donaire et al. (2023) for the star formation rates, and in Watts et al. (2023) for the stellar surface densities. The only difference between the data presented in previous VERTICO papers and here is that we have reduced the molecular-gas surface densities by a factor of 1.36 to remove the “helium contribution,” as we are specifically interested in H₂.

2.2. Simulations

The IllustrisTNG model of galaxy formation (Weinberger et al. 2017; Pillepich et al. 2018) comprises key descriptions of astrophysical processes, including gas cooling, star and black hole formation, stellar evolution and feedback, feedback from active galactic nuclei (AGNs), and more, all within a Λ CDM

cosmological, magnetohydrodynamic framework with the moving-mesh AREPO code (Springel 2010). Simulations of various box sizes and resolutions have been run with the IllustrisTNG model, all of which carry identical parameters for both the sub-resolution physical prescriptions and cosmology, with the latter based on Planck Collaboration et al. (2016). We use the TNG50 simulation (Nelson et al. 2019a; Pillepich et al. 2019) in this paper, which has a periodic box length of ~ 50 cMpc and baryonic mass resolution of $8.5 \times 10^4 M_\odot$. Galaxy subhalos in TNG are identified with SUBFIND (Springel et al. 2001; Dolag et al. 2009).

The H I and H₂ properties of gas cells in TNG were calculated in post-processing (Diemer et al. 2018; Stevens et al. 2019b). In this paper, we use the decomposition based on Gnedin & Draine (2014) as described in Stevens et al. (2019b).

The integrated H I and H₂ properties of TNG100 galaxies and their trends with environment have been explored in depth (Diemer et al. 2019; Stevens et al. 2019b, 2021), but the same is not true in the literature¹⁷ for TNG50 (but see Boselli et al. 2023). In brief, after mock-observing the simulated galaxies to match survey specifications, Stevens et al. (2019b, 2021) show that TNG100 quantitatively reproduces gas-fraction trends seen with ALFALFA, xGASS, and xCOLD GASS (i.e., from the results of Brown et al. 2017; Saintonge et al. 2017; Catinella et al. 2018). To show that the gas fractions of TNG50 and TNG100 are consistent, we compare the H I and H₂ fractions of the simulations in Figure 1. To approximately match the galaxies in the observational samples described in Section 2.1, we exclusively consider TNG galaxies at $z = 0$ with $m_* \geq 10^9 M_\odot$ and $\text{SFR} \geq 0.05 M_\odot \text{yr}^{-1}$ (based on measurements internal to the “BaryMP” radius of Stevens et al. 2014, also referred to as the “inherent” properties in Stevens et al. 2019b) in this figure and throughout this Letter. We also exclude any galaxy with a dark-matter fraction below 5% to conservatively remove non-cosmological objects (see the criteria in Nelson et al. 2019b). This totals 2479 galaxies from TNG50. Other than a small systematic increase in H₂ fraction for TNG50, the two simulations are well aligned. There is generally good agreement between global H I and H₂ gas fractions in TNG100 and low-redshift observations (e.g., ALFALFA, xGASS, and xCOLD GASS; Stevens et al. 2019a; Diemer et al. 2019), especially after mock-observing TNG galaxies to survey specifications. For the purposes of this paper, we infer by extension that TNG50 sufficiently agrees with observations. We note that in Figure 1 the TNG50 cluster sample has higher gas fractions than their VERTICO counterparts at fixed stellar mass, particularly where $m_* \leq 10^{10} M_\odot$. Due to the small number statistics in this regime, we caution against overinterpretation, yet it is possible that this is due to a systematic difference between the simulated and observed samples. For example, environmental processes in TNG50 may not be regulating gas content in lower stellar mass simulated galaxies to the same extent as for the observed galaxies.

We create mock surface density maps of H I, H₂, and stellar mass for each TNG galaxy in our sample. These maps are matched to the specifications of the HERACLES and VERTICO data by convolving each map at the simulation’s native resolution with a Gaussian kernel with a full width at half maximum of 1.2 kpc, and then resampling with square

¹⁷ Figures published in Diemer et al. (2019) with TNG100 and TNG300 have been reproduced with TNG50 at <http://www.benediktdiemer.com/data/hi-h2-in-illustris/>.

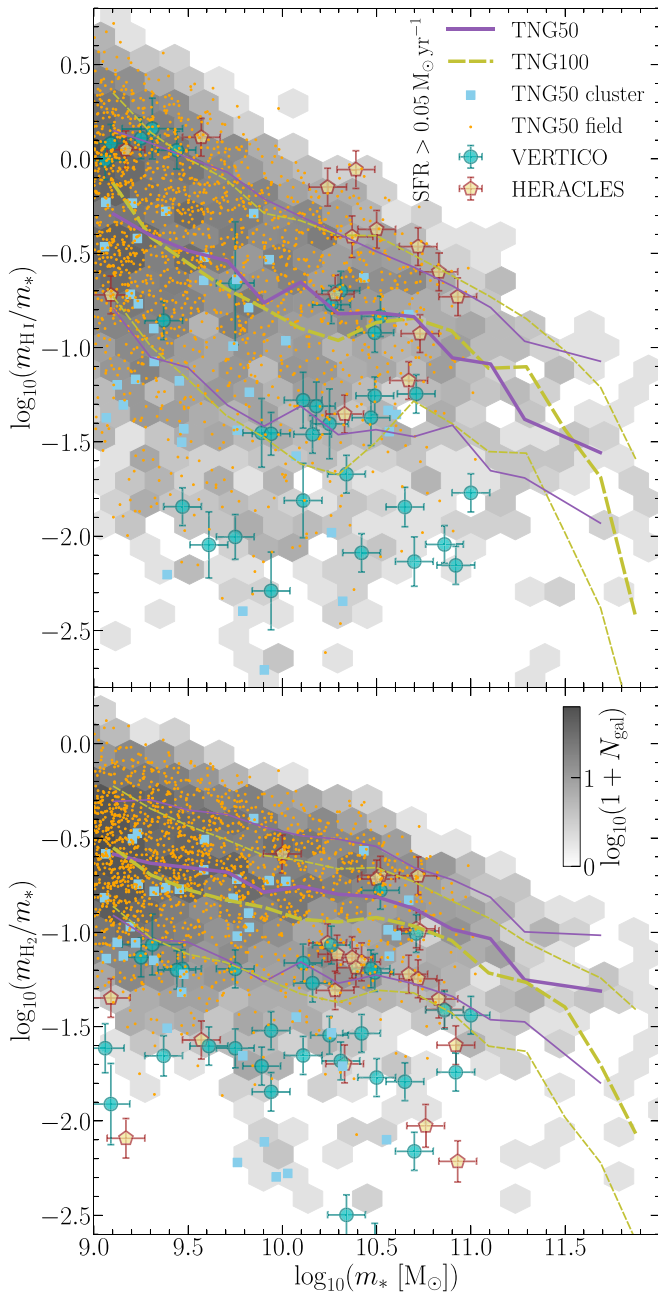


Figure 1. The H I (top panel) and H₂ (bottom panel) fractions of TNG50 and TNG100 galaxies as a function of stellar mass at $z=0$. Only galaxies with $m_* \geq 10^9 M_\odot$ and $\text{SFR} \geq 0.05 M_\odot \text{ yr}^{-1}$ are included (without any environmental subsampling). Hex bins show the number density of TNG50 galaxies. Lines are the running median (thick) and 16th and 84th percentiles (thin) for TNG50 (solid) and TNG100 (dashed). Points with approximate errors compare the VERTICO and HERACLES galaxies that we use in this paper (a subset of the full surveys; see Figure 1 of Zabel et al. 2022). We show these observational data for reference, but we do *not* necessarily expect the simulation medians to align closely with them (but they should be closer to HERACLES than VERTICO). Individual points from our TNG50 cluster and field samples, shown, can be respectively compared to VERTICO and HERACLES.

pixels of length 0.65 kpc. This physical scale matches the resolution of the observational data. Each map is made face-on using the angular-momentum vector of all neutral gas (any gas that is not ionized) inside the “BaryMP” radius (Stevens et al. 2014), under the assumption that the observations have been correctly projected.

We separate TNG50 galaxies into two subsamples after applying the above cuts. The “field” sample, intended to be comparable to HERACLES, is selected to contain only central galaxies (those in the most massive SUBFIND subhalo) in haloes with virial mass $M_{200c} \leq 10^{12.2} M_\odot$. The field sample totals 1739 galaxies with an average number of 1514 pixels with $\Sigma_* > 1 M_\odot \text{ pc}^{-2}$ per galaxy. The “cluster” sample, comparable to VERTICO, contains only satellites (galaxies that are not centrals) in the simulation’s two clusters¹⁸ with $M_{200c} \gtrsim 10^{14} M_\odot$. The most massive cluster, with $M_{200c} = 1.8 \times 10^{14} M_\odot$, is very similar in mass to Virgo ($1.4\text{--}4.2 \times 10^{14} M_\odot$; see Table 1 of Boselli et al. 2018 and references therein). The other TNG50 cluster is about half this mass ($M_{200c} = 9.4 \times 10^{13} M_\odot$) but has a different dynamical state and has already been justified as a Virgo analog by Joshi et al. (2021). The cluster sample totals 41 galaxies with an average of 1725 pixels with $\Sigma_* > 1 M_\odot \text{ pc}^{-2}$ per galaxy. The higher pixel count per galaxy in the cluster sample reflects its higher average stellar mass (see the distribution of TNG50 points in Figure 1).

3. Results

We explore how the resolved gas–stellar surface density scaling relations of galaxies are affected by environment, which we do in two steps. First, we compare sample-averaged scaling relations between the field and cluster samples in TNG50 to those of HERACLES and VERTICO. Second, we present the resolved relations of individual cluster galaxies, assessing how the relations change with global H I deficiencies, and comparing analogous galaxies between TNG50 and VERTICO.

3.1. Sample Averages

Our first aim is to see if the *average* behavior of kiloparsec-scale gas in TNG50 reflects that of reality in both the field and cluster environments. In Figure 2, we present the pixel-based relations of Σ_{HI} and Σ_{H_2} as a function of Σ_* . The pixels for all galaxies in the TNG50 cluster sample are grouped together, as are those in the field sample. The same grouping strategy applies for HERACLES and VERTICO. To demonstrate that the preference of HERACLES galaxies to have $m_* \gtrsim 10^{10} M_\odot$ (seen in Figure 1) does not affect our comparison, we add results to Figure 2 for a TNG50 field subsample where we have excluded galaxies with $m_* \leq 10^{10} M_\odot$. We exclude the resolved molecular Kennicutt–Schmidt relation ($\Sigma_{\text{H}_2} - \Sigma_{\text{SFR}}$) from Figure 2 as we find that the relation is independent of environment to first order in TNG50. Indeed, Jiménez-Donaire et al. (2023) have also shown that this is true in observations. Because of this, we also choose not to include the resolved star-forming main sequence ($\Sigma_* - \Sigma_{\text{SFR}}$) as it presents similar information to the resolved molecular-gas main sequence in TNG50, as it does in observations ($\Sigma_* - \Sigma_{\text{H}_2}$; addressed further in Brown et al. 2023). See Motwani et al. (2022) for further analysis on kiloparsec-scale Σ_{SFR} in TNG50.

¹⁸ Images of these clusters (and much more) can be found at <https://www.tng-project.org/media/>. We could obtain many more Virgo-mass clusters using TNG100 or TNG300, but the main advantage of TNG50 is its superior resolution. For a pixel of size (650 pc)², a surface density of $1 M_\odot \text{ pc}^{-2}$ — which we want to resolve down to — contains the equivalent mass of ~ 5 gas elements in TNG50. In TNG100, this would be less than half a gas element. We therefore stick to TNG50 to minimize the potential for numerical effects to skew our results.

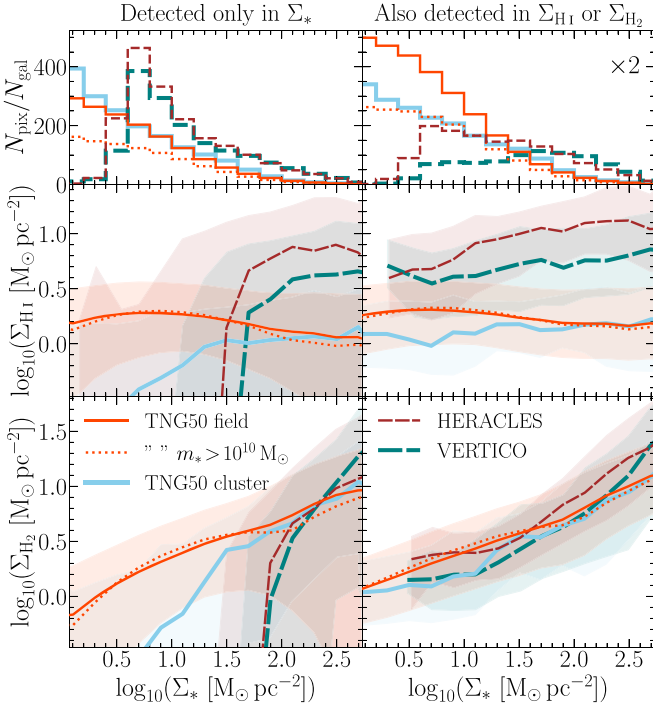


Figure 2. Resolved scaling relations for TNG50 galaxies per their field and cluster samples (and a high-mass field subsample), compared respectively with HERACLES and VERTICO. Lines are running medians in 0.2 dex bins of Σ_* . Shaded regions cover the 16th to 84th percentiles (not shown for the high-mass field subsample). The left column accounts for all pixels in both the observations (provided they were detected in stellar emission) and simulations, setting non-detections in either Σ_{HI} or Σ_{H_2} in the observations to zero, which are accounted for in the percentiles. The right column removes any non-detections in the observations by cutting out any pixels that would fall below the axes as plotted. The lower boundary of each axis represents the 1st percentile of all gas-detected pixels (irrespective of whether the pixel is a detection in Σ_*) across both observational surveys. This boundary also represents the cut in gas surface density applied to TNG50 in the right-hand panels, as to emulate a detection threshold. The top two panels show the one-dimensional histograms of Σ_* for pixels in each sample, normalized by the number of galaxies in that sample. The y-axis in the top right panel is stretched by a factor of 2 for clarity.

The left column of panels in Figure 2 accounts for all pixels with Σ_* detections, regardless of whether they were detected in HI or H₂. For the purposes of calculating percentiles, gas non-detections are assumed to have zero mass. The sharp downturn in the VERTICO and HERACLES medians from right to left is simply representative of the threshold surface densities needed for gas to be detected in those surveys.

From these panels, we can immediately identify that TNG50 quantitatively reproduces the correlation between Σ_{H_2} and Σ_* , while the $\Sigma_{\text{HI}}-\Sigma_*$ relation in the simulation is systematically offset to lower Σ_{HI} values. VERTICO cluster galaxies are systematically suppressed in Σ_{HI} by a factor of ~ 2 at fixed Σ_* relative to HERACLES but not significantly for Σ_{H_2} . This is in line with the findings of Watts et al. (2023) even though we are including lower-mass galaxies than in that study.

By contrast to the observations, the Σ_{HI} medians are not parallel for the field and cluster samples in TNG50, instead converging at high Σ_* . Both Σ_{HI} and Σ_{H_2} become increasingly divergent between the TNG50 cluster and field samples at $\Sigma_* \lesssim 30 M_\odot \text{pc}^{-2}$. This average behavior is typical of disk truncation, which one would expect from processes like ram pressure stripping that affect the cluster galaxies.

TNG50 galaxies in field and cluster samples are systematically low in Σ_{HI} relative to observations and exhibit little to no environmental dependence at high Σ_* (the centers of galaxies). This central deficit in HI appears to be widespread in TNG50, a finding described in Gebek et al. (2023), and also seen in TNG100 by Diemer et al. (2019) and in Figures A1 and A2 of Stevens et al. (2019a). A similar outcome has also been found for the EAGLE simulation (Bahé et al. 2016). Discussion in Section 4.5.2 of Diemer et al. (2019) and Section 4.3 of Gebek et al. (2023) describes how (some) central HI deficits in TNG are likely the result of high ionized fractions in the interstellar medium and AGN feedback removing gas from galaxy centers (also see Stevens et al. 2019b, 2021). We also note that among all the post-processing methods used to decompose neutral gas in TNG into its atomic and molecular components, all have molecular fractions that asymptote to 1 at high densities, evidently leading to a relatively low saturation density for HI (see Diemer et al. 2018).

There are also fewer pixels per galaxy at high Σ_* in TNG50 than observations, as seen in the top panels of Figure 2. This implies that galaxy centers are generally underdense in the simulation. Numerical heating of stellar particles plays a role here in artificially decreasing central stellar densities (see Ludlow et al. 2021). This same effect has a minimal influence on gas, suggesting pixels in TNG50 galaxies are leftward of where they should be in Figure 2. The low gas densities, combined with this systematic underestimation of Σ_* in the centers of galaxies, are likely also the reason that we do not see an environmental influence on Σ_{HI} at high values of Σ_* compared to observations.

It is important to assess what the role of pixels undetected in gas have on (i) the average behavior of the observations and (ii) the comparison with TNG described above. To this end, we compare gas-detected pixels in both the observations and simulations in the right-hand panels of Figure 2. We apply a lower limit for Σ_{HI} and Σ_{H_2} equal to the minimum value in the respective axes in the figure to emulate a detection threshold for TNG. While the median $\Sigma_*-\Sigma_{\text{H}_2}$ relations for Σ_{H_2} detections in TNG50 and observations are in reasonable agreement, the systematic deficit in TNG's Σ_{HI} relative to observations is even more stark than before. The latter suggests that TNG galaxies are already suppressed in Σ_{HI} at high Σ_* before falling into the cluster. There is minimal suppression in their central Σ_{HI} thereafter, while the observations instead show a clear suppression. However, because the TNG galaxies are selected to be star forming, and only 41 of those meet our cluster criteria, this does *not* automatically mean the correct qualitative effect of environment on kiloparsec-scale gas is absent in the simulation, as we explore in Section 3.2.

3.2. Individual Cluster Galaxies

The ensemble relations above demonstrate the systematic underestimation of Σ_{HI} at fixed stellar density in TNG50 with respect to the observations. But ensemble relations are merely the superposition of individual relations. Thus, to establish if TNG50 can reproduce the resolved effects of environmental mechanisms on individual galaxies' gas content reported by Watts et al. (2023), we need to explore their *individual* $\Sigma_*-\Sigma_{\text{HI}}$ and $\Sigma_*-\Sigma_{\text{H}_2}$ sequences.

In a similar fashion to Watts et al. (2023), we rank-order our TNG50 cluster sample by HI deficiency (HI-def for short) and show their individual $\Sigma_*-\Sigma_{\text{HI}}$ and $\Sigma_*-\Sigma_{\text{H}_2}$ sequences in

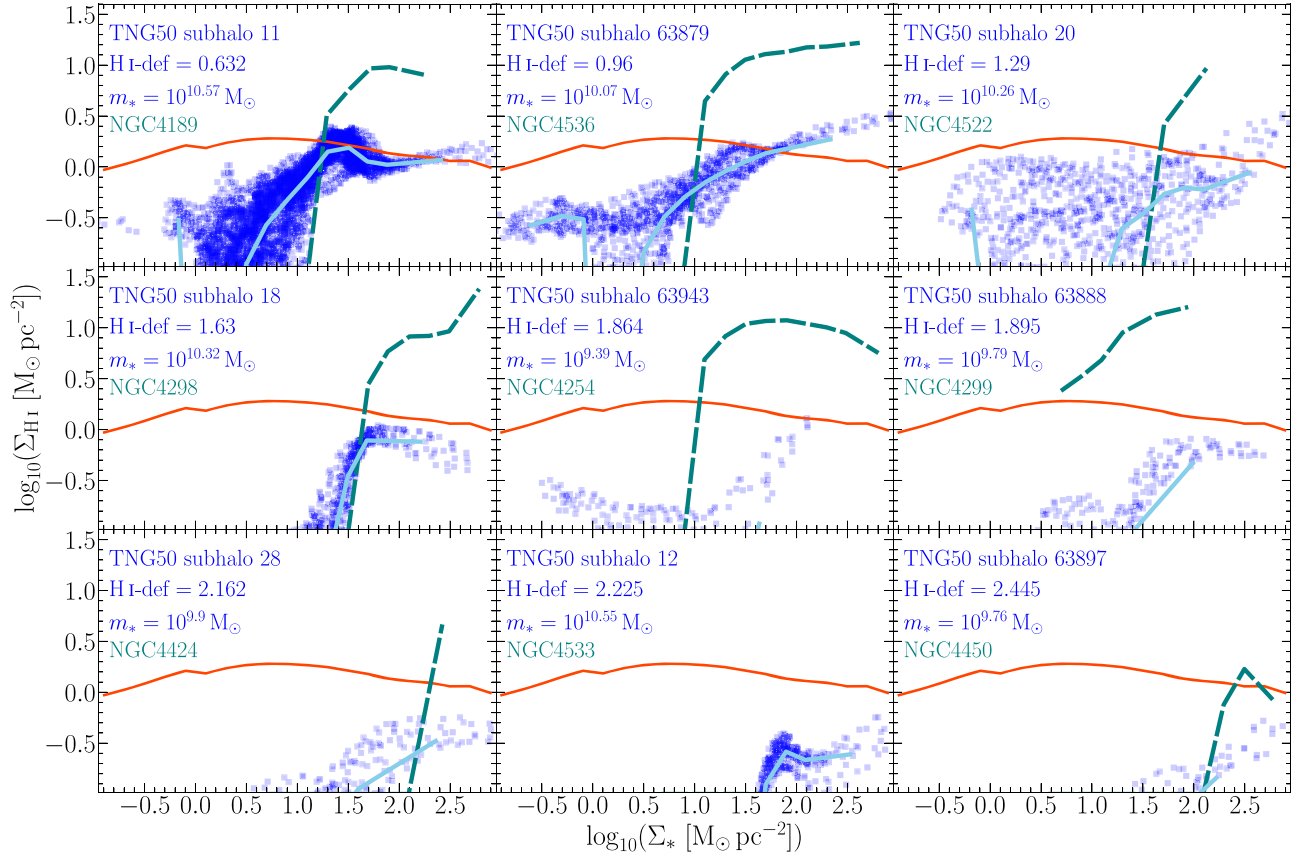


Figure 3. Individual H I sequences for the nine most H I-deficient galaxies among VERTICO analogs in TNG50. Points are pixels from the TNG50 galaxies, with thick solid lines the running median of those points. The thin, solid red line that repeats in each panel is the median for the TNG50 field sample. Each dashed line is the running median for the VERTICO galaxy that the TNG50 galaxy is matched to, based on its stellar mass and distance from the star-forming main sequence. NGC4533 lacks any detected resolved H I. The lower bound of the y-axis in each panel is ~ 0.5 dex lower than what is detected in VERTICO galaxies.

Figures 3 and 4, respectively. H I deficiency is often used as a proxy for how processed a galaxy has been by its environment, provided H I-def > 0.3 . Here, H I-def is defined as the logarithmic deviation in expected H I mass at fixed stellar mass, relative to the median of TNG50 field galaxies (shown in Figure 1).¹⁹ Each pixel for each TNG50 galaxy in Figures 3 and 4 is shown along with their running median. The running median for the whole TNG50 field sample (a “control”) is shown along with one analog VERTICO galaxy, matched according to its stellar mass and distance from the (integrated) star-forming main sequence. For the real galaxies, we use the main sequence of Leroy et al. (2019), which we write in terms of specific star formation rate:

$$\log_{10}\left(\frac{\text{sSFR}_{\text{MS}}^{\text{L19}}}{\text{yr}^{-1}}\right) = -0.346 \log_{10}\left(\frac{m_*}{M_{\odot}}\right) - 6.652. \quad (1)$$

For TNG galaxies, we iteratively perform a least-squares straight-line fit to $\log_{10}(m_*) - \log_{10}(\text{sSFR})$, removing outliers of $> 3\sigma$ each time to ensure we do not accidentally include quenched galaxies, until the fit converges. The resulting fit is

$$\log_{10}\left(\frac{\text{sSFR}_{\text{MS}}^{\text{TNG}}}{\text{yr}^{-1}}\right) = -0.159 \log_{10}\left(\frac{m_*}{M_{\odot}}\right) - 8.427. \quad (2)$$

¹⁹ This is a different definition of H I-def to that used in Watts et al. (2023), but it serves the same function.

The vector length between the TNG50 and VERTICO matched pairs is always shorter than 0.3 dex in this parameter space. Although H I deficiency and distance from the main sequence are physically correlated, we note that this method does *not* mean that the H I deficiencies of the paired VERTICO and TNG50 galaxies are the same. There are 13 galaxies in the TNG50 cluster sample that both have H I-def > 0.3 dex and have VERTICO analogs, of which the nine with the highest H I-def are shown in Figures 3 and 4.

Figure 3 demonstrates that when examining the most environmentally affected TNG galaxies, the simulation *does* reproduce the *qualitative* results of VERTICO per Watts et al. (2023), i.e., that (i) gas disks are truncated to higher Σ_* for higher H I-def and (ii) central $\Sigma_{\text{H I}}$ decreases for high H I-def. This did not appear to be the case in Figure 2 because 28 of the 41 galaxies in the TNG50 cluster sample are either H I-normal, i.e., they have H I-def < 0.3 , and/or have no (unique) analog in VERTICO.

Figure 4 shows the $\Sigma_* - \Sigma_{\text{H}_2}$ sequences for the same galaxies as in Figure 3. We see truncation occurring at the same Σ_* in both $\Sigma_{\text{H I}}$ and Σ_{H_2} , and we see a suppression in central Σ_{H_2} for the most H I-deficient galaxies. These results are again qualitatively in line with that reported for VERTICO in Watts et al. (2023).

The fact that the majority of galaxies in the TNG50 cluster sample are unaffected by their environment (i.e., 28 of the 41 galaxies are H I-normal, a much larger fraction than in the observations) is because many TNG galaxies that are strongly

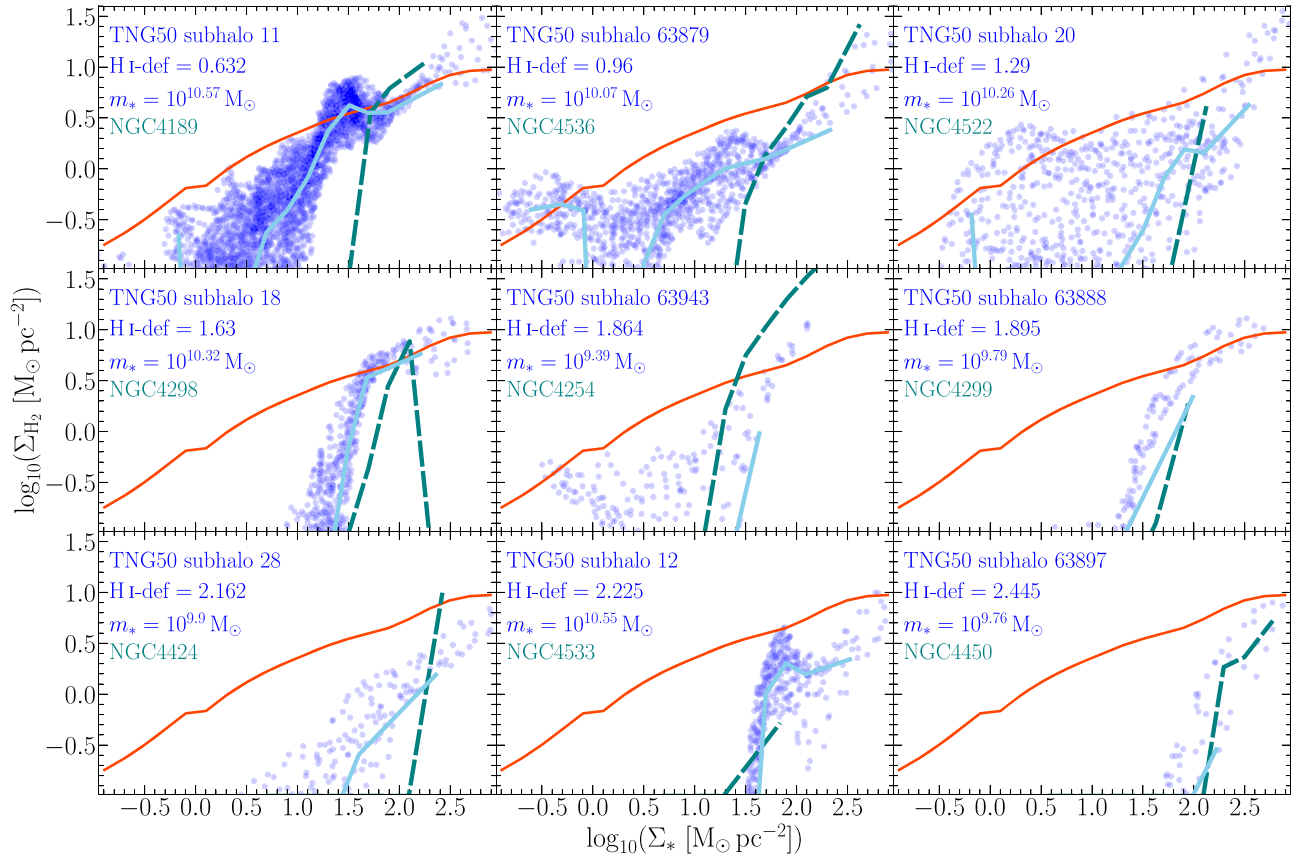


Figure 4. Same as Figure 3 but for the resolved molecular-gas main sequence.

affected by a cluster environment belong to a subhalo that is devoid of gas cells entirely,²⁰ especially at low stellar masses (see Section 5.2 of Diemer et al. 2019; Figure 9 of Stevens et al. 2021). Naturally, such galaxies, where the environmental influence on gas content is greatest, cannot be included in this work. While the improved resolution of TNG50 relative to earlier simulations in the suite certainly combats this issue, numerical simulations are always limited by discretization. Only with enough dense gas elements are the hydrodynamical forces of environment reliable in the simulation. In essence, this means there is a narrow window of opportunity to catch simulated galaxies experiencing the onset of environmental effects. No analogous limitation exists for observed galaxies. This might explain why the TNG50 cluster sample is small in number, despite having two clusters of comparable mass to Virgo. In future work, this issue can be mitigated by using more snapshots to catch the moment of interest for each infalling satellite galaxy.

4. Summary

TNG50 *quantitatively* reproduces the Σ_* - Σ_{H_2} relation found in observations in both cluster and field samples. The Σ_* - Σ_{HI} relation, on the other hand, is found to be endemically gas poor at fixed Σ_* with respect to the observations. In addition, we find that the kiloparsec-scale effects of a Virgo-like environment on satellite galaxies' HI and H₂ gas content is *qualitatively* recovered by TNG50 at $z = 0$. Gas disks are not

only truncated more the more they have been affected by their environment, but their central gas densities are also relatively suppressed. However, this effect is likely quantitatively weaker than in reality because the central gas surface densities of TNG50 galaxies, particularly in HI, are systematically low relative to observations, irrespective of environment.

With this baseline performance of TNG50 established, it opens the door to using the TNG simulations to show how the resolved-gas scaling relations of galaxies change after infall into a cluster or otherwise dense environment. Such an experiment is crucial to reinforce the theoretical interpretation of the empirical results of VERTICO, which must rely on conjecture in describing cluster galaxies' histories.

Acknowledgments

Parts of this research were funded by a Research Collaboration Award from The University of Western Australia. A.R.H. S. is a grateful recipient of the Jim Buckee Fellowship at ICRAR-UWA. T.B. acknowledges support from the National Research Council of Canada via the Plaskett Fellowship of the Dominion Astrophysical Observatory. V.V. acknowledges support from the scholarship ANID-FULBRIGHT BIO 2016-56160020 and funding from NRAO Student Observing Support (SOS) - SOSPADA-015. D.N. acknowledges funding from the Deutsche Forschungsgemeinschaft (DFG) through an Emmy Noether Research Group (grant number NE 2441/1-1). Y.B. acknowledges funding from the Dutch Research Organisation (NWO) through Veni grant number 639.041.751 and financial support from the Swiss National Science Foundation (SNSF) under project 200021_213076.

²⁰ Gas cells in AREPO are volume filling, meaning gas is always present everywhere. But that does not mean gas is specifically associated with substructure or a galaxy.

This paper makes use of the following ALMA data:

1. ADS/JAO.ALMA #2019.1.00763.L
2. ADS/JAO.ALMA #2017.1.00886.L
3. ADS/JAO.ALMA #2016.1.00912.S
4. ADS/JAO.ALMA #2015.1.00956.S














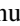
ALMA is a partnership of ESO (representing its member states), NSF (USA) and NINS (Japan), together with NRC (Canada), MOST and ASIAA (Taiwan), and KASI (Republic of Korea), in cooperation with the Republic of Chile. The Joint ALMA Observatory is operated by ESO, AUI/NRAO and NAOJ. The National Radio Astronomy Observatory is a facility of the National Science Foundation operated under cooperative agreement by Associated Universities, Inc.




This research made use of data provided by the NASA/IPAC Infrared Science Archive, which is funded by the National Aeronautics and Space Administration and operated by the California Institute of Technology.

The authors acknowledge the use of the Canadian Advanced Network for Astronomy Research (CANFAR) Science Platform. Our work used the facilities of the Canadian Astronomy Data Center, operated by the National Research Council of Canada with the support of the Canadian Space Agency, and CANFAR, a consortium that serves the data-intensive storage, access, and processing needs of university groups and centers engaged in astronomy research (Gaudet et al. 2010).

Facilities: ALMA, VLA, GALEX, Sloan, WISE.

ORCID iDs

Adam R. H. Stevens  <https://orcid.org/0000-0003-1908-2168>
 Toby Brown  <https://orcid.org/0000-0003-1845-0934>
 Benedikt Diemer  <https://orcid.org/0000-0001-9568-7287>
 Annalisa Pillepich  <https://orcid.org/0000-0003-1065-9274>
 Lars Hernquist  <https://orcid.org/0000-0001-6950-1629>
 Dylan Nelson  <https://orcid.org/0000-0001-8421-5890>
 Alessandro Boselli  <https://orcid.org/0000-0002-9795-6433>
 Timothy A. Davis  <https://orcid.org/0000-0003-4932-9379>
 Pascal J. Elahi  <https://orcid.org/0000-0002-6154-7224>
 Sara L. Ellison  <https://orcid.org/0000-0002-1768-1899>
 María J. Jiménez-Donaire  <https://orcid.org/0000-0002-9165-8080>
 Ian D. Roberts  <https://orcid.org/0000-0002-0692-0911>
 Kristine Spekkens  <https://orcid.org/0000-0002-0956-7949>
 Vicente Villanueva  <https://orcid.org/0000-0002-5877-379X>

Adam B. Watts  <https://orcid.org/0000-0002-9405-0687>
 Christine D. Wilson  <https://orcid.org/0000-0001-5817-0991>
 Nikki Zabel  <https://orcid.org/0000-0001-7732-5338>

References

- Bahé, Y. M., Crain, R. A., Kauffmann, G., et al. 2016, *MNRAS*, 456, 1115
 Boselli, A., Fossati, M., Cote, P., et al. 2023, *A&A*, 675, A123
 Boselli, A., Fossati, M., Ferrarese, L., et al. 2018, *A&A*, 614, A56
 Brown, T., Catinella, B., Cortese, L., et al. 2017, *MNRAS*, 466, 1275
 Brown, T., Roberts, I. D., Thorp, M., et al. 2023, *ApJ*, 956, 37
 Brown, T., Wilson, C. D., Zabel, N., et al. 2021, *ApJS*, 257, 21
 Catinella, B., Saintonge, A., Janowiecki, S., et al. 2018, *MNRAS*, 476, 875
 Chung, A., van Gorkom, J. H., Kenney, J. D. P., Crowl, H., & Vollmer, B. 2009, *AJ*, 138, 1741
 Cortese, L., Catinella, B., & Smith, R. 2021, *PASA*, 38, e035
 Diemer, B., Stevens, A. R. H., Forbes, J. C., et al. 2018, *ApJS*, 238, 33
 Diemer, B., Stevens, A. R. H., Lagos, C. d. P., et al. 2019, *MNRAS*, 487, 1529
 Dolag, K., Borgani, S., Murante, G., & Springel, V. 2009, *MNRAS*, 399, 497
 Gaudet, S., Hill, N., Armstrong, P., et al. 2010, *Proc. SPIE*, 7740, 774011
 Gebek, A., Baes, M., Diemer, B., et al. 2023, *MNRAS*, 521, 5645
 Gnedin, N. Y., & Draine, B. T. 2014, *ApJ*, 795, 37
 Jiménez-Donaire, M. J., Brown, T., Wilson, C. D., et al. 2023, *A&A*, 671, A3
 Joshi, G. D., Pillepich, A., Nelson, D., et al. 2021, *MNRAS*, 508, 1652
 Leroy, A. K., Sandstrom, K. M., Lang, D., et al. 2019, *ApJS*, 244, 24
 Leroy, A. K., Walter, F., Bigiel, F., et al. 2009, *AJ*, 137, 4670
 Ludlow, A. D., Fall, S. M., Schaye, J., & Obreschkow, D. 2021, *MNRAS*, 508, 5114
 Motwani, B., Genel, S., Bryan, G. L., et al. 2022, *ApJ*, 926, 139
 Nelson, D., Pillepich, A., Springel, V., et al. 2019a, *MNRAS*, 490, 3234
 Nelson, D., Springel, V., Pillepich, A., et al. 2019b, *ComAC*, 6, 2
 Pillepich, A., Nelson, D., Springel, V., et al. 2019, *MNRAS*, 490, 3196
 Pillepich, A., Springel, V., Nelson, D., et al. 2018, *MNRAS*, 473, 4077
 Planck Collaboration, Ade, P. A. R., Aghanim, N., et al. 2016, *A&A*, 594, A13
 Saintonge, A., Catinella, B., Tacconi, L. J., et al. 2017, *ApJS*, 233, 22
 Springel, V. 2010, *MNRAS*, 401, 791
 Springel, V., White, S. D. M., Tormen, G., & Kauffmann, G. 2001, *MNRAS*, 328, 726
 Stevens, A. R. H., & Brown, T. 2017, *MNRAS*, 471, 447
 Stevens, A. R. H., Diemer, B., Lagos, C. d. P., et al. 2019a, *MNRAS*, 490, 96
 Stevens, A. R. H., Diemer, B., Lagos, C. d. P., et al. 2019b, *MNRAS*, 483, 5334
 Stevens, A. R. H., Lagos, C. d. P., Cortese, L., et al. 2021, *MNRAS*, 502, 3158
 Stevens, A. R. H., Martig, M., Croton, D. J., & Feng, Y. 2014, *MNRAS*, 445, 239
 Villanueva, V., Bolatto, A. D., Vogel, S., et al. 2022, *ApJ*, 940, 176
 Walter, F., Brinks, E., de Blok, W. J. G., et al. 2008, *AJ*, 136, 2563
 Watts, A. B., Cortese, L., Catinella, B., et al. 2023, *PASA*, 40, e017
 Weinberger, R., Springel, V., Hernquist, L., et al. 2017, *MNRAS*, 465, 3291
 Xie, L., De Lucia, G., Hirschmann, M., & Fontanot, F. 2020, *MNRAS*, 498, 4327
 Yun, K., Pillepich, A., Zinger, E., et al. 2019, *MNRAS*, 483, 1042
 Zabel, N., Brown, T., Wilson, C. D., et al. 2022, *ApJ*, 933, 10